UCLA
UCLA Previously Published Works

Title

Iron-decorated nitrogen-rich carbons as efficient oxygen reduction electrocatalysts for Zn–air batteries

Permalink

https://escholarship.org/uc/item/7x74q5xw

Journal

Nanoscale, 10(36)

ISSN

2040-3364

Authors

Liu, Zhuang
Liu, Jing
Wu, Hao Bin
et al.

Publication Date

2018-09-20

DOI

10.1039/c8nr04627a

Peer reviewed

Iron-Decorated Nitrogen-Rich Carbons as Efficient Oxygen Reduction Electrocatalysts for Zn-Air Battery

Zhuang Liu[#a], **Jing Liu**[#a], **Hao Bin Wu**[b], **Gurong Shen**[a], **Zaiyuan Le**[a], **Gen Chen**[a], and **Yunfeng Lu**[a]

[a]Department of Chemical and Biomolecular Engineering, University of California, Los Angeles, CA 90095, USA. luucla@ucla.edu

[b]School of Materials Science and Engineering, Zhejiang University, Hangzhou 310027, China. hbwu@zju.edu.cn

[#] These authors contributed equally to this work.

Abstract

A low-cost and scalable method has been developed to synthesize Fe-decorated N-rich carbon electrocatalysts for oxygen reduction reaction (ORR) based on pyrolysis of metal carbonyls containing metal-organic frameworks (MOFs). Such method simultaneously optimizes the Fe-related active sites and the porous structure of the catalysts. Accodingly, the best-performing Fe-NC-900-M catalyst shows excellent ORR activity with a half-wave potential of 0.91 V vs. RHE, exceeding that of 40% Pt/C catalyst in alkaline media. Furthermore, the zinc-air battery constructed with Fe-NC-900-M as cathode catalyst exhibits high open-circuit voltage (1.5 V) and peak power density (271 mW cm^{-2}), which outperforms that of most zinc-air batteries with noble-metal free ORR catalysts.

Metal-air batteries are promising electrochemical devices for energy conversion owing to their high energy density and environmental friendliness. However, their performance has been limited by the sluggish oxygen reduction reaction (ORR) at the air cathodes.[1–3] Although Pt-based catalysts show high catalytic activity towards ORR, the scarcity and high cost prevent their large-scale applications. Thus, developing non-Pt ORR catalysts appears the ultimate solution to broaden the use of metal-air batteries.[4–8]

During the past decade, a wide variety of materials have been studied as non-Pt ORR catalysts.[9–19] Among them, "iron-nitrogen-carbon (Fe-N-C)" catalysts, which are typically prepared by pyrolyzing Fe, N, C-containing precursors exhibit the most promising activity.[2, 6, 20] However, though Fe-N$_x$ moieties are generally accepted as the major active site, the function of Fe/Fe$_3$C nanoparticles in Fe-N-C catalysts has been debated. While some works report severe reduction in the catalysts activity upon the presence of Fe/Fe$_3$C nanoparticles, other studies show that these nanoparticles may increase the activity of Fe-N$_x$ through electronic interaction or acting as co-active sites.[21–25]

The complex nature of active centers place difficulties in the controllable synthesis of the catalysts and precise manipulation of the structure/composition at nanometer scale.[26–29] To boost the electrocatalytic activity, it is essential for the catalysts to possess high density of active sites, large surface area, and desired porous structure.[19, 30–38] However, these features are generally achieved using costly organometallic compounds and hard templates, as well as tedious post treatment, compromising the economy and scalability.[2, 39–41]

Herein, we demonstrate an economic and easy-scalable approach to synthesize non-precious metal ORR electrocatalysts by pyrolyzing metal-organic frameworks (MOFs)-iron carbonyl (Fe(CO)$_5$) complex. As shown in Scheme 1, nanocrystals of a N-rich MOF (ZIF-8) are used as a porous host to absorb and stabilize iron carbonyl at ambient temperature. Fe-decorated N-rich carbon (Fe-NC) catalysts are then obtained by directly pyrolyzing the iron carbonyl containing ZIF-8 (ZIF-8/Fe). During the pyrolysis, Fe(CO)$_5$ reacts homogeneously with the ZIF-8 scaffold, leading to the uniform decoration of Fe-related species on the N-rich porous carbon derived from ZIF-8. The in-situ generated hierarchically porous structure could host the active sites by micropores and promote charge/mass transport by meso-/macropores, providing a large amount of easily accessible ORR active sites.[30] In virtue of these advantageous features, the optimized Fe-NC catalyst exhibits excellent ORR activity with a half-wave potential of 0.91 V (vs. reversible hydrogen electrode, RHE), exceeding that of the benchmark 40% Pt/C catalyst. Furthermore, the zinc-air battery constructed with our Fe-NC catalyst at cathode, exhibits high open-circuit voltage (1.5 V) and peak power density (271 mW cm^{-2}), which outperforms that of most zinc-air batteries with non-precious metal catalysts (NPMCs) reported so far.

Note that MOFs have been used as precursors for various electrochemically active mateirlas, [42–45] including ORR catalysts. For example, N-doped carbons with Co-based moieties have been prepared by pyrolyzing Co based MOFs (e.g., ZIF-67 and ZIF-9).[16, 46–48] However, using MOFs as a single precursor for M-N-C catalysts provides quite limited capability to control the composition. Thus, in several studies aiming to synthesize Fe-N-C catalysts using MOFs, additional Fe salts and costly N-containing chelating compounds are indispensable. Such components were generally mixed and reacted with bulky MOF particles, which increase the cost and likely cause inhomogeneity in the catalysts.[20, 49–50] Alternatively, partially replacing the pristine metal centers in MOFs (e.g., Fe-doped ZIF-8) offers a limited capability to manipulate the composition of MOF precursors.[51–52] In contrast, the approach developed in this work is cost-effective and easily scalable. Moreover, tuning the metal centers of the catalyst could be easily achieved by incorporating other metal carbonyls, offering the possibility to further enhance the catalytic activity and durability.

Uniform ZIF-8 nanocrystals with size of around 80 nm (Fig. S1, see the Electronic Supplementary Information (ESI)) were first synthesized by a simple and scalable co-precipitation method.[53] After thoroughly removing the solvent, ZIF-8 nanocrystals were directly dispersed in iron carbonyl, a light-orange-colored liquid. After stirring for 4 h, the resulting iron carbonyl decorated ZIF-8 (ZIF-8/Fe) well retains the crystal structure of the pristine ZIF-8 without any visible impurity from the powder X-ray diffraction (XRD) patterns (Fig. 1a). However, an obvious change in color, from white of ZIF-8 to light brown of ZIF-8/Fe was observed (insets of Figure 1a). The successful incorporation of Fe in

ZIF-8/Fe is further verified by energy-dispersive X-ray spectroscopy (EDS) analysis (Fig. S2, see the ESI). Additionally, transmission electron microsope (TEM) images of the ZIF-8/Fe reveals the well preserved polyhedral morphology of ZIF-8 with a rougher surface (Fig. S3, see the ESI). On the basis of the above observation, we conclude that iron carbonyl would be mostly absorbed by the porous structure of ZIF-8. Due to the strong interaction between these two components, the highly volatile and reactive iron carbonyl could be stabilized and participate in the formation of active sites upon heating.[54]

Thermogravimetric analysis (TGA) shows that ZIF-8 starts to decompose and carbonize at around 620°C, followed by continuous weight loss at high temperature due to vaporization of Zn and loss of unstable species (Fig. S4a, see the ESI). While for ZIF-8/Fe, the gradual weight loss at low temperature is likely caused by the decomposition of iron carbonyl. It is also noted that the presence of Fe triggers the carbonization at a lower temperature of 570 °C (Figure S4b, see the ESI), manifesting the interaction between ZIF-8 and Fe during pyrolysis. Thus, Fe-NC catalysts were obtained by pyrolysis of ZIF-8/Fe in N_2 at 800, 900 and 1000 °C (generating Fe-NC-800, Fe-NC-900 and Fe-NC-1000 respectively) to optimize its composition and porous structure. As shown in Fig. 1b, energy-dispersive X-ray spectroscopy (EDS) analysis shows that Zn has been completely removed during the heat treatment except for some minimal residual in Fe-NC-800. As the annealing temperature increases, the atomic contents of N and O decrease from 17.8 to 4.5 at.% and from 9.3 to 1.7 at.%, respectively, while the content of Fe remains in the range of 1.6–2.2 at.%. The XRD patterns (Fig. 1c) indicate that the Fe-NC samples consist of amorphous carbon as characterized by the broad humps at around 26°. In Fe-NC-900, minor diffraction peaks due to crystalline moieties are observed at around 44°. The diffraction peaks become much more pronounced in Fe-NC-1000, which are identified as Fe and Fe_3C. Formation of such crystalline phases are common in Fe-N-C catalysts, and they might also contribute to the catalytic activity for ORR.[17, 21] Yet no Fe-related peaks is observed in the XRD pattern of Fe-NC-800, which may because that Fe atoms in this sample mostly exists in a non-crystalline form.

Specific surface area and pore structure of the Fe-NC catalysts are characterized by N_2 adsorption-desorption isotherms (Fig. S5, see the ESI). All three samples exhibit hierarchical pore structure consisting of micro-, meso- and macro- pores. The specific surface area and pore volume contributed from micropores and meso-/macropores are compared for the three catalysts in Fig. 1d. At an annealing temperature of 800 °C, the porosity of Fe-NC-800 is not fully developed, resulting in a moderate surface area of 290 m^2 g^{-1}.

Raising the temperature to 900 °C increases the surface area of Fe-NC-900 to 526 m^2 g^{-1} with a high microporous surface area of over 300 m^2 g^{-1}, as well as increased pore volume. Further increasing the temperature to 1000 °C somehow creates more meso-/macropores in Fe-NC-1000 yet substantially decreases the microporosity, resulting in a decreased surface area of 444 m^2 g^{-1}.

Scanning electron microscope (SEM) and transmission electron microscope (TEM) were employed to investigate the Fe-NC catalysts. All of the samples show similar morphology

under SEM observation with interconnected nanoparticles originated from the ZIF-8 nanocrystals (Fig. S6, see the ESI). However, TEM images in Fig. 2 show different nanostructure of these samples. In line with the XRD result, no crystalline species are found in Fe-NC-800 (Fig. 2a and b). The interconnected carbon particles form a disordered meso-/macroporous structure, and each carbon particle exhibits a highly microporous texture. For Fe-NC-900, similar hierarchical porous structure is observed with increased porosity (Fig. 2c), which is expected from the loss of unstable species at high temperature. Moreover, crystalline Fe/Fe$_3$C nanoparticles with small size below 30 nm could be identified as black spots in the TEM images (arrow in Fig. 2d), which are embedded in the carbon matrix. At a higher temperature of 1000 $^\circ$C, the Fe/Fe$_3$C nanoparticles further migrate, coalesce and grow into larger particles (Fig. 2e), leaving behind many empty graphitic shells (arrow in Fig. 2f). Such catalytic formation of graphitic carbon is common in the presence of Fe,[6, 15] and it is accounted for the increased meso-/macroporosity and elimination of micropores in Fe-NC-1000.

X-ray photoelectron spectroscopy (XPS) was performed to analyze the binding states of N and Fe of the Fe-NC catalysts (Fig. 3a and b). The N 1s spectra show the existence of pyrrolic (400.2 eV) and pyridinic (398.4 eV) nitrogen, while the second peak, whose ratio decreases upon increasing temperature, might also include a contribution from nitrogen of Fe-N$_x$ moieties.[15, 30, 55] The surface Fe content is found to be 4.25, 3.36 and 1.22 at.% for Fe-NC-800, 900, 1000 respectively. No signals of zero-valence Fe was observed in the Fe 2p spectra of the Fe-NC catalysts, and the peak at around 710 eV can be attributed to the Fe in Fe-N$_x$ moieties, which agrees well with the TEM observation that the formed Fe particles in Fe-NC catalysts are coated with carbon.[56] High temperature treatment aggregates Fe atoms to form nanocrystals, removes N, O atoms and recovers defects in the carbon structure. Which might enhance the electronic conductivity but reduce the amount of ORR active sites. Therefore, a compromise should be made to achieve the optimal performance as discussed shortly.

The electrocatalytic performance of Fe-NC catalysts for ORR was evaluated in 0.1 M NaOH solution using a rotating disk electrode (RDE). The polarization curves shown in Fig. 3c indicate that all of the three Fe-NC catalysts are highly active towards ORR. Among them, Fe-NC-900 shows the best electrocatalytic performance, which is approaching that of the benchmark Pt/C catalyst (40 wt%, Johnson Matthey, with a Pt loading of 50 μg cm^{-2}). A high half-wave potential ($E_{1/2}$) of 0.88V (vs. RHE) is obtained, together with an increased limiting current. In contrast, NC-900, prepared by pyrolyzing ZIF-8 at 900 $^\circ$C without iron carbonyl displays much inferior catalytic activity, confirming the critical role of Fe in forming active sites. Tafel plots (Fig. S7, see the ESI) provide additional information regarding the electrocatalytic behaviors of the different catalysts. Fe-NC-900 and Fe-NC-1000 show small Tafel slopes of 62 and 59 mV dec^{-1} respectively, which are comparable to that of Pt/C (56 mV dec^{-1}). Fe-NC-800 however, exhibits a higher Tafel slope of 98 mV dec^{-1}, implying that the rate-determinant step might involve both charge transfer and the transport of reaction intermediates.[6]

The onset potentials, half-wave potentials and Tafel slopes of the Fe-NC and Pt/C catalysts are summarized for better comparison in Fig. 3d. Interestingly, a higher temperature of

pyrolysis results in a lower onset potential and a lower Tafel slope of the corresponding Fe-NC catalysts, for which several reasons can be assumed. First, the Fe-NC sample prepared at lower temperature exhibits higher N content, especially Fe-NC-800 exhibits the highest N content of 17.8 at.%, which may promote the formation of non-crystalline active sites like Fe-N_x. Such effect is supported by the absence of Fe-based particles and the highest surface Fe content in Fe-NC-800, which gives rise to its highest onset potential.[20] On the other hand, increase of annealing temperature in the case of Fe-NC-900 and Fe-NC-1000 substantially reduces N-doping and promotes the growth of Fe-based nanocrystallites. Which reduces surface Fe-N_x and lowers the onset potential. Nevertheless, higher temperature creates rich meso-/macropores (Fig. 1d) and removes defects in the carbon matrix. As a result, the mass and electron transport are facilitated in Fe-NC-900 and Fe-NC-1000, which attribute to their lower Tafel slopes.

In principle, an ideal catalyst should have a high onset potential and a small Tafel slope in order to achieve high current density with low over-potential. However, we find that the pyrolysis temperature shows contradictory effects on the Fe-NC catalysts, and consequently, a compromise results in the highest $E_{1/2}$ of Fe-NC-900. The high catalytic activity of Fe-NC-900 could also be understood by its high micro-pore surface area and electrochemical surface area (ECSA) (Fig. S8, see the ESI) that host rich accessible Fe-N_x sites. Moreover, the stability of Fe-NC-900 was evaluated by continuous cyclic voltammetry (CV) scans between 0.6–1.0 V vs. RHE in O_2 saturated electrolyte.[17] The polarization curve of Fe-NC-900 after 5000 potential cycles well overlaps with the original one, with only a small shift of around 5 mV in $E_{1/2}$ (Fig. S9, see the ESI), proving its excellent stability.

Having optimized the pyrolysis temperature, we further investigated the possibility to improve the catalyst by increasing Fe content, which may increase the density of active sites. Specifically, the stirring time of ZIF-8 in iron carbonyl was extended from the original 4 h for Fe-NC-900 to 8 h for medium Fe loading (Fe-NC-900-M) and 12 h for high Fe loading (Fe-NC-900-H). As shown in Fig. 4a, Fe-NC-900-M shows greatly improved catalytic performance in terms of a much higher half-wave potential of 0.91V, exceeding that of the benchmark Pt/C catalyst ($E_{1/2}$ = 0.90 V) and most of the NPMCs reported so far (Table S1, see the ESI). Whereas further increasing the Fe content significantly decreases the activity of Fe-NC-900-H (Fig. S10, see the ESI). XRD and TEM results suggest that Fe-NC-900-M generally retains the nanostructure of Fe-NC-900 (Fig. S11, see the ESI). However, excess loading of Fe produces abundant large Fe particles and catalyzes the growth of carbon nanotubes in Fe-NC-900-H, which might eliminate the Fe-N_x active sites residing in the pristine microporous carbon structure. In addition, the apparent catalytic performance can also be improved by increasing the catalyst loading on RDE. For example, tripling the loading of Fe-NC-900-M to 0.75 mg cm^{-2}, a value comparable to those of many reported NPMCs,[6, 18, 20] will dramatically increase the ORR limiting current (denoted as Fe-NC-900-M-HL in Fig. S12, see the ESI).

To investigate the function of different components of Fe-NC catalysts in catalyzing ORR, Fe-NC-900-M was washed with 0.5 M H_2SO_4 to remove Fe/Fe_3C nanocrystallites while retaining the Fe-N_x moieties (Fig. S13–15, see the ESI). As shown in Figure 4a, rotating ring-disk electrode (RRDE) measurements reveals that the electron transfer number of Fe-

NC-900-M is greater than 3.9 in the whole potential range, indicating near-perfect selectivity of 4 e- pathway. On the other hand, the nanoparticle-free Fe-NC-900-M-AW exhibits much lower $E_{1/2}$ (0.83 eV) and electron transfer number (~3.7), which are still much higher than those of the Fe-free NC-900. We also tested the RRDE performance of Fe-NC-900-M with the presence of NaSCN in the electrolyte, where SCN- ion is known to poison Fe-N_x sites.[57] As shown in Fig. S16 (see the ESI), the $E_{1/2}$ of Fe-NC-900-M decreases dramatically by about 40 mV, and the electron transfer number drops to about 3.7 after adding 1 mM NaSCN, which is still superior to Fe-free sample. The above results together conclude that the high performance of Fe-NC-900-M for ORR should be attributed to both Fe-N_x moieties and Fe/Fe_3C nanoparticles. [21–23]

To further demonstrate the potential application of Fe-NC ORR catalyst, we assembled prototype zinc-air battery using Fe-NC-900-M as the electrocatalyst in air cathode. Commercial 40% Pt/C catalyst was also tested under the same condition for comparison. As shown in Fig. 4b, the zinc-air battery constructed with Fe-NC-900-M as cathode catalyst exhibits an open circuit voltage of 1.5 V. Under a constant discharge current of 44 mA cm^{-2}, a stable voltage output of 1.22 V is maintained for over 4h without notable degradation (Fig. 4c). The polarization curves of zinc-air battery gives a peak power density of 271 mW cm^{-2}, which exceeds that with 40% Pt/C catalyst (242 mW cm^{-2}) and most NPMCs reported so far (Table S2, see the ESI).[26, 58–64]

Additionally, the present method can also be easily extended to synthesize M-NC catalysts with other transition metals, by using the corresponding metal carbonyls. Though preliminary results show inferior activity of other M-NC catalysts (Fig. S17, see the ESI), incorporating multiple metal incorporating multiple metal centers in the present Fe-NC catalysts might further improve its activity.[6]

Conclusions

In summary, we have developed a low-cost and easy-scalable method to synthesize Fe-NC catalysts based on the direct pyrolysis of iron carbonyl decorated ZIF-8. Increasing pyrolysis temperature is revealed to lower the onset potential as well as the Tafel slope of the catalyst, as a result of the altered chemical composition and porous structure. The optimized Fe-NC-900-M catalyst shows excellent electro-catalytic activity for ORR with a half-wave potential of 0.91 V, which is also attributed to the synergistic effect between Fe-N_x and Fe/Fe_3C nanocrystallites of the catalyst. Furthermore, the zinc-air battery constructed with Fe-NC-900-M as cathode catalyst exhibits high open-circuit voltage (1.5 V) and peak power density (271 mW cm^{-2}), which outperforms that of 40% Pt/C catalyst and most noble-metal free ORR catalysts reported so far. The Fe-NC catalysts are promising candidates to replace Pt-based catalysts, and would play an important role in the development of high-performance and low-cost metal-air batteries

Supplementary Material

Refer to Web version on PubMed Central for supplementary material.

Author Manuscript

Acknowledgements

References

1. Cheng F, Chen J, Chem. Soc. Rev, 2008, 41, 2172.

2. Lefèvre M, Proietti E, Jaouen F, Dodelet J-P, Science, 2009, 324, 71. [PubMed: 19342583]

3. Suntivich J, Gasteiger HA, Yabuuchi N, Nakanishi H, Goodenough JB, Shao-Horn Y, Nat. Chem, 2011, 3, 546. [PubMed: 21697876]

4. Cao R, Lee J-S, Liu M, Cho J, Adv. Energy Mater, 2012, 2, 816.

5. Shao M, Chang Q, Dodelet J-P, Chenitz R, Chem. Rev, 2016, 116, 3594. [PubMed: 26886420]

6. Wu G, More KL, Johnston CM, Zelenay P, Science, 2011, 332, 443. [PubMed: 21512028]

7. Zhu C, Li H, Fu S, Du D and Lin Y, Chem. Soc. Rev, 2016, 45, 517. [PubMed: 26658546]

8. Guo D, Shibuya R, Akiba C, Saji S, Kondo T and Nakamura J, Science, 2016, 351, 361. [PubMed: 26798009]

9. Gong K, Du F, Xia Z, Durstock M and Dai L, Science, 2009, 323, 760. [PubMed: 19197058]

10. Pei Z, Li H, Huang Y, Xue Q, Huang Y, Zhu M, Wang Z and Zhi C, Energy Environ. Sci, 2017, 10, 742.

11. Ma TY, Ran J, Dai S, Jaroniec M and Qiao SZ, Angew. Chem. Int. Ed, 2015, 54, 4646.

12. Chen P, Zhou T, Xing L, Xu K, Tong Y, Xie H, Zhang L, Yan W, Chu W, Wu C and Xie Y, Angew. Chem. Int. Ed, 2017, 56, 610.

13. Liang Y, Li Y, Wang H, Zhou J, Wang J, Regier T and Dai H, Nat. Mater, 2011, 10, 780. [PubMed: 21822263]

14. Fu J, Hassan FM, Li J, Lee DU, Ghannoum AR. Lui G, Hoque MA and Chen Z, Adv. Mater, 2016, 28, 6421. [PubMed: 27197721]

15. Wu Z-Y, Xu X-X, Hu B-C, Liang H-W, Lin Y, Chen L-F and Yu S-H, Angew. Chem. Int. Ed, 2015, 54, 8179.

16. Xia BY, Yan Y, Li N, Wu HB, Lou XW and Wang X, Nat. Energy, 2016, 1, 15006.

17. Hu Y, Jensen JO, Zhang W, Cleemann LN, Xing W, Bjerrum NJ and Li Q, Angew. Chem. Int. Ed, 2014, 53, 3675.

18. Zan Y, Zhang Z, Liu H, D M, and Wang F, J. Mater. Chem. A, 2017, 5, 24329.

19. Jaouen F, Proietti E, Lefevre M, Chenitz R, Dodelet J-P, Wu G, Chung HT, Johnston CM and Zelenay P, Energy Environ. Sci, 2011, 4, 114.

20. Zitolo A, Goellner V, Armel V, Sougrati M-T, Mineva T, Stievano L, Fonda E and Jaouen F, Nat. Mater, 2015, 14, 937. [PubMed: 26259106]

21. Jiang W-J, Gu L, Li L, Zhang Y, Zhang X, Zhang L-J, Wang J-Q, Hu J-S, Wei Z, Wan L-J, J. Am. Chem. Soc, 2016, 138, 3570. [PubMed: 26906342]

22. Sa YJ, Seo D-J, Woo J, Lim JT, Cheon JY, Yang SY, Lee JM, Kang D, Shin TJ, Shin HS, Jeong HY, Kim CS, Kim MG, Kim T-Y and Joo SH, J. Am. Chem. Soc, 2016, 138, 15046. [PubMed: 27750429]

23. Liu Z, Sun F, Gu L, Chen G, Shang T, Liu J, Le Z, Li X, Wu HB, Lu Y, Adv. Energy Mater, 2017, 7, 1701154.

24. Chen Y, Ji S, Wang Y, Dong J, Chen W, Li Z, Shen R, Zheng L, Zhuang Z, Wang D, Li Y, Angew. Chem. Int. Ed, 2017, 56, 6937.

25. Deng D, Yu L, Chen X, Wang G, Jin L, Pan X, Deng J, Sun G, Bao X, Angew. Chem. Int. Ed, 2013, 52, 371.

26. Pan J, Xu Y, Yang H, Dong Z, Liu H, Xia B, Adv. Sci, 2018, 5, 1700691.

27. Li Y, Dai H, Chem. Soc. Rev, 2014, 43, 5257. [PubMed: 24926965]

28. Han Y, Wang Y, Chen W, Xu R, Zheng L, Zhang J, Luo J, Shen R, Zhu Y, Cheong W, Chen C, Peng Q, Wang D, Li Y, J. Am. Chem. Soc, 2017, 139, 17269. [PubMed: 29108411]

29. Han A, Chen W, Zhang S, Zhang M, Han Y, Zhang J, Ji S, Zheng L, Wang Y, Gu L, Chen C, Peng Q, Wang D, Li Y, Adv. Mater, 2018, 30, 1706508.

30. Liang H-W, Wei W, Wu Z-S, Feng X, Müllen K, J. Am. Chem. Soc, 2013,135, 16002. [PubMed: 24128393]

31. Cheon JY, Kim T, Choi Y, Jeong HY, Kim MG, Sa YJ, Kim J, Lee Z, Yang T, Kwon K, Terasaki O, Park G, Adzic RR, Joo SH, Sci. Rep, 2013, 3, 2715. [PubMed: 24056308]

32. Liang J, Zhou RF, Chen XM, Tang YH, Qiao SZ, Adv. Mater, 2014, 26, 6074. [PubMed: 25042569]

33. Zhou R, Qiao SZ, Chem. Commun, 2015, 51, 7516.

34. Cheon JY, Kim K, Sa YJ, Sahgong SH, Hong Y, Woo J, Yim S, Jeong HY, Kim Y, Joo SH, Adv. Energy Mater, 2016, 6, 1501794.

35. Li J, Hou P, Shi C, Zhao S, Tang D, Cheng M, Liu C, Cheng H, Carbon, 2016, 109, 632.

36. Peng S, Jiang H, Zhang Y, Yang L, Wang S, Deng W, Tan Y, J. Mater. Chem. A, 2016, 4 3678.

37. Ahn SH, Yu X, Manthiram A, Adv. Mater, 2017, 29, 1606534.

38. Woo J, Sa YJ, Kim JH, Lee H, Pak C, Joo SH, ChemElectroChem, 2018, 5, 1928.

39. Wang M, Qian T, Zhou J and Yan C, ACS Appl. Mater. Interfaces, 2017, 9, 5213. [PubMed: 28106376]

40. Ma L, Chen S, Pei Z, Huang Y, Liang G, Mo F, Yang Q, Su J, Gao Y, Zapien JA and Zhi C, ACS Nano, 2018, 12, 1949. [PubMed: 29432686]

41. Li Z, Li G, Jiang L, Li J, Sun G, Xia C, Li F, Angew. Chem. Int. Ed, 2015, 54, 1494.

42. Zhang H, Nai J, Yu L and Lou XW, Joule, 2017, 1, 77.

43. Wang H, Zhu Q-L, Zou R and Xu Q, Chem, 2017, 2, 52.

44. Wu HB and Lou XW, Sci. Adv, 2017, 3, eaap9252.

45. Hu H, Han L, Yu M, Wang Z and Lou XW, Energy Environ. Sci, 2016, 9, 107.

46. Chaikittisilp W, Torad NL, Li C, Imura M, Suzuki N, Ishihara S, Ariga K and Yamauchi Y, Chem. Eur. J, 2014, 20, 4217. [PubMed: 24623613]

47. Hou Y, Wen Z, Cui S, Ci S, Mao S and Chen J, Adv. Funct. Mater, 2015, 25, 872.

48. Shang L, Yu H, Huang X, Bian T, Shi R, Zhao Y, Waterhouse GIN, Wu L-Z, Tung C-H and Zhang T, Adv. Mater, 2016, 28, 1668. [PubMed: 26677131]

49. Lai Q, Zheng L, Liang Y, He J, Zhao J and Chen J, ACS Catal, 2017, 7, 1655.

50. Liu Y, Zeng X, Wang W and Cao D, Adv. Funct. Mater, 2018, 28, 1704537.

51. Liu T, Zhao P, Hua X, Luo W, Chen S and Cheng G, J. Mater. Chem. A, 2016, 4, 11357.

52. Wang X, Zhang H, Lin H, Gupta S, Wang C, Tao Z, Fu H, Wang T, Zheng J, Wu G and Li X, Nano Energy, 2016, 25, 110.

53. Cravillon J, Nayuk R, Springer S, Feldhoff A, Huber K and Wiebcke M, Chem. Mater, 2011, 23, 2130.

54. Li W-P, Su C-H, Tsao L-C, Chang C-T, Hsu Y-P, Yeh C-S, ACS Nano, 2016, 10, 11027. [PubMed: 28024357]

55. Koslowski U, Herrmann I, Bogdanoff P, Barkschat C, Fiechter S, Iwata N, Takahashi H, Nishikori H, ECS Trans, 2008, 13, 125.

56. Cao R, Thapa R, Kim H, Xu X, Kim MG, Li Q, Park N, Liu M, Cho J, Nat. Commun, 2013, 4, 2076. [PubMed: 23797710]

57. Wang Q, Zhou Z-Y, Lai Y-J, You Y, Liu J-G, Wu X-L, Terefe E, Chen C, Song L, Rauf M, Tian N and Sun S-G, J. Am. Chem. Soc, 2014, 136, 10882. [PubMed: 25033100]

58. Wang T, Kou Z, Mu S, Liu J, He D, Amiinu IS, Meng W, Zhou K, Luo Z, Chaemchuen S and Verpoort F, Adv. Funct. Mater, 2018, 28, 1705048.

59. Pei Z, Tang Z, Liu Z, Huang Y, Wang Y, Li H, Xue Q, Zhu M, Tang D and Zhi C, J. Mater. Chem. A, 2018, 6, 489.

60. Anandhababu G, Abbas SC, Lv J, Ding K, Liu Q, Babu DD, Huang Y, Xie J, Wu M, Wang Y, Dalton Trans, 2017, 46, 1803. [PubMed: 28102397]

61. Zhu J, Zhou H, Zhang C, Zhang J, Mu S, Nanoscale, 2017, 9, 13257. [PubMed: 28853479]

62. Liang H-W, Wu Z-Y, Chen L-F, Li C, Yu S-H, Nano Energy, 2015, 11, 366.

63. Zang Y, Zhang H, Zhang X, Liu R, Liu S, Wang G, Zhang Y, Zhao H, Nano Research, 2016, 9, 2123.

64. Su C-Y, Cheng H, Li W, Liu Z-Q, Li N, Hou Z, Bai F-Q, Zhang H-X and Ma T-Y, Adv. Energy Mater, 2017, 7, 1602420.
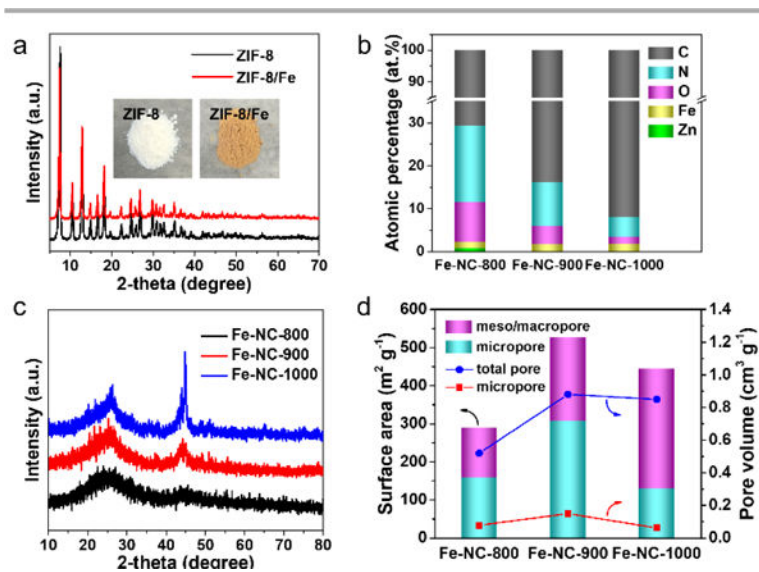
Fig. 1.
(a) XRD patterns of ZIF-8 and ZIF-8/Fe (insets show the digital photos of the samples). (b) Elemental composition of the Fe-NC catalysts determined by EDS. (c) XRD patterns of the Fe-NC catalysts prepared at different temperatures. (d) Comparison of the specific surface area and pore volume contributed from micropores and meso/macropores of the Fe-NC catalysts.
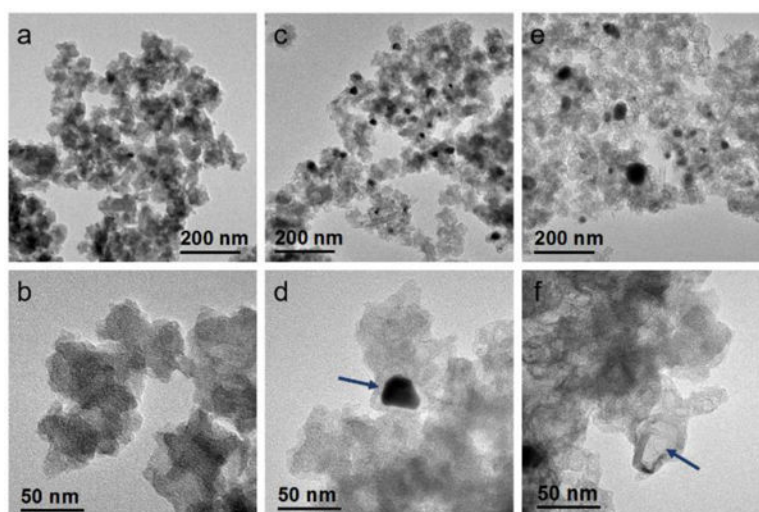
Fig. 2.
TEM images of (a, b) Fe-NC-800, (c, d) Fe-NC-900 (arrow in d indicates the Fe/Fe$_3$C crystalline nanoparticle), (e, f) Fe-NC-1000 (arrow in f indicates the cage-like structure).
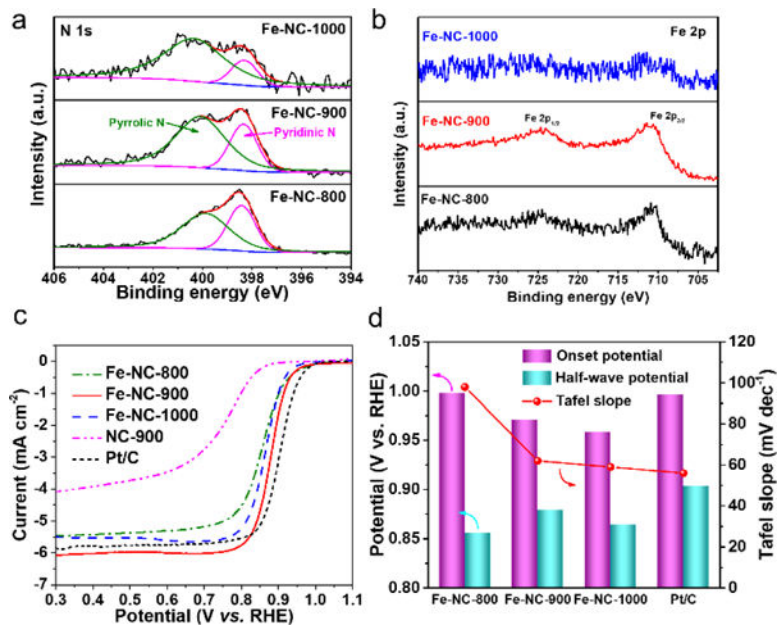
Fig. 3.
(a, b) XPS N1s and Fe2p spectra of Fe-NC catalysts prepared at different temperature. (c) Polarization curves of Fe-NC catalysts prepared at different temperature (loading: 0.25 mg cm^{-2}), NC-900 (loading: 0.25 mg cm^{-2}) and commercial 40 wt% Pt/C catalyst (Johnson Matthey, 50 gPt cm^{-2}) in 0.1 M NaOH at 1600 rpm. (d) Comparison of onset potential, half-wave potential and Tafel slope of different Fe-NC and Pt/C catalysts.
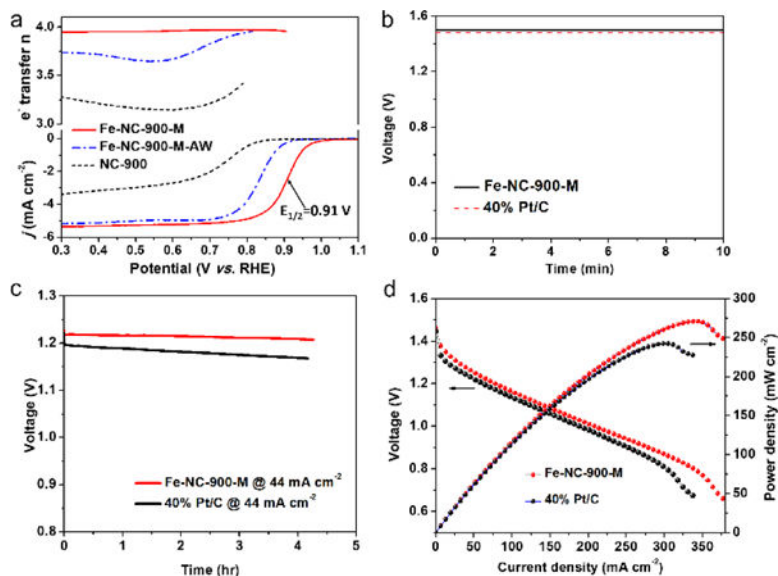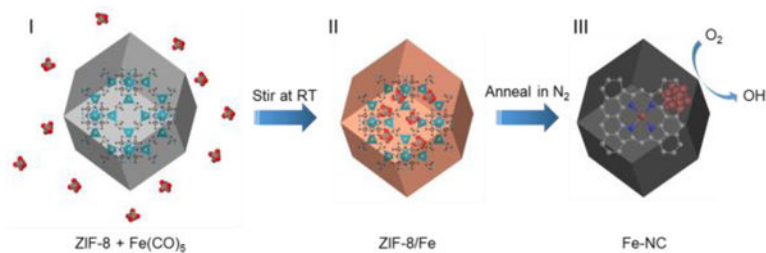
Fig. 4.
(a) Polarization curves and the corresponding electron transfer number of Fe-NC-900-M, Fe-NC-900-M-AW and NC-900 (loading: 0.25 mg cm^{-2}) in 0.1 M NaOH at 1600 rpm. (b) Open-circuit voltage, (c) discharge curves at 44 mA cm^{-2}, (d) polarization curves and the corresponding power density plot of the Zn-air batteries constructed with Fe-NC-900-M and 40% Pt/C as cathode catalysts.

Scheme 1.
Schematic illustration of the synthesis of Fe-NC catalysts. (I) ZIF-8 nanocrystals (grey polyhedron; the crystal structure of ZIF-8 is superimposed) dispersed in Fe(CO)5 (surrounding molecules). (II) ZIF-8/Fe precursor (orange polyhedron) with Fe(CO)5 confined in the porous framework (shown in the superimposed image). (III) Fe-NC catalyst particles (black polyhedron) with hierarchical pores (possible structures of Fe-containing moieties are superimposed; brown: iron; grey: carbon; blue: nitrogen).